Effect of relative humidity on drying-induced damage in concrete
A comparative study of digital image correlation and lattice modelling

Gao, Peng; Chen , Yang; Huang, Haoliang; Qian, Zhiwei; Schlangen, Erik; Wei, Jiangxiong; Yu, Qijun

DOI
10.1016/j.matdes.2020.109128

Publication date
2020

Document Version
Final published version

Published in
Materials and Design

Citation (APA)
Gao, P., Chen , Y., Huang, H., Qian, Z., Schlangen, E., Wei, J., & Yu, Q. (2020). Effect of relative humidity on drying-induced damage in concrete: A comparative study of digital image correlation and lattice modelling. *Materials and Design*, *196*, Article 109128. https://doi.org/10.1016/j.matdes.2020.109128

Materials and Design 196 (2020) 109128

Contents lists available at ScienceDirect

Materials and Design

journal homepage: www.elsevier.com/locate/matdes

Effect of relative humidity on drying-induced damage in concrete: A comparative study of digital image correlation and lattice modelling

Peng Gao [a], Yang Chen [a,c], Haoliang Huang [a,b], Zhiwei Qian [d], Erik Schlangen [e], Jiangxiong Wei [a,b,*], Qijun Yu [a,b]

[a] School of Materials Science and Engineering, South China University of Technology, 510640 Guangzhou, People's Republic of China
[b] Guangdong Low Carbon Technologies Engineering Centre for Building Materials, 510640 Guangzhou, People's Republic of China
[c] Guangdong Provincial Academy of Building Research Group Co., Ltd., 510500 Guangzhou, People's Republic of China
[d] FEMRIS, The Hague, 2497, CJ, the Netherlands
[e] Microlab, Faculty of Civil Engineering and Geosciences, Delft University of Technology, 2628, CN, Delft, the Netherlands

HIGHLIGHTS

- Drying-induced damage patterns in concrete can be identified using the principal strains determined by the digital image correlation.
- Damage index calculated from the principal strains is proportional to the total area of drying-induced microcracks in concrete.
- Relative humidity equal or lower than 55% could lead to relatively large damage index and high cracking risk in concrete

GRAPHICAL ABSTRACT

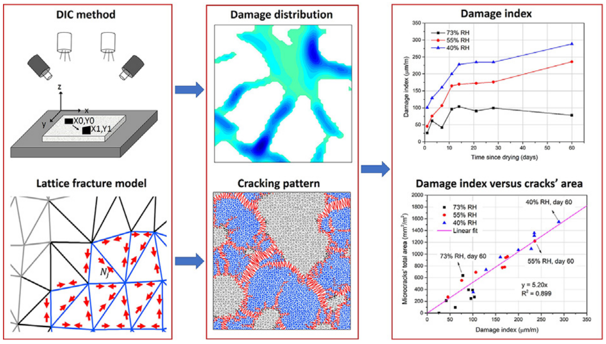

ARTICLE INFO

Article history:
Received 18 May 2020
Received in revised form 13 August 2020
Accepted 5 September 2020
Available online 09 September 2020

Keywords:
Drying shrinkage
Relative humidity
Microcracks
Damage index
DIC
Lattice modelling

ABSTRACT

To assess the effect of relative humidity (RH) on drying-induced damage in concrete, the non-uniform strains and microcracks in concrete under different RH conditions were obtained using the digital image correlation (DIC) technique and lattice fracture model. The simulated non-uniform displacements were consistent with those captured using DIC. A new damage index was proposed by considering all the subsets with equivalent strain larger than the threshold tensile strength. The calculated damage index showed good correlation with the microcracks' total area and indicated that RH equal or lower than 55% could cause relatively high cracking risk. This work provides an attractive method for quantifying drying-induced damage in concrete using the DIC technique.

1. Introduction

Drying shrinkage of concrete is an important issue because it can produce cracks in concrete structures [1]. On a meso-scale, concrete mainly consists of mortar and coarse aggregates. The main phases of the mortar are fine aggregates and cement paste. Because the cement paste is a multi-scale porous phase comprising capillary pores and gel pores [2], the moisture in the cement paste will evaporate when the relative humidity (RH) in the environment decreases. Consequently, stresses in the cement phase such as capillary pressure, disjoining pressure and surface tension will change [3,4], leading to the drying shrinkage of mortar phase. On a meso-scale, the mortar phase shrinkage is

---

* Corresponding author at: School of Materials Science and Engineering, South China University of Technology, 510640 Guangzhou, People's Republic of China.
E-mail address: jxwei@scut.edu.cn (J. Wei).

https://doi.org/10.1016/j.matdes.2020.109128

responsible for the bulk drying shrinkage of concrete, with the coarse aggregates having a restraining effect on the mortar phase shrinkage [5,6]. The restraining effect of the coarse aggregates results in both compressive and tensile stresses in the mortar phase during the shrinkage [7,8]. Once these drying-induced stresses overcome the strength of concrete, microcracks will form, which could cause serious deterioration in concrete structures [1].

The drying-induced strains, stresses and microcracks in concrete are non-uniform because both the spatial distribution and shape of the coarse aggregates are generally heterogeneous [9]. With developments in the testing and modelling of cement-based materials in recent years, new research has emerged focused on the non-uniform behaviour of concrete. For example, digital image correlation (DIC) is an optical method that estimates the full-field deformation of materials by mathematically analysing the digital images of specimens captured before and after the deformation [10–12]. This technique has the advantages of simple experimental set-up and preparation, low environmental sensitivity, and easy and automatic processing [13–16]. In recent years, many studies used DIC to determine the non-uniform deformations of cement-based materials [16–28]. Studying drying shrinkage in cement-based materials, Lagier et al. [17], Mauroux et al. [18], and Maruyama et al. [19–21] used DIC to determine the non-uniform strains and attempted to identify the patterns of drying-induced damage in concrete. In a previous study by our group [16], the DIC technique was used to evaluate the influence of the size and volume fraction of coarse aggregates on the heterogenous characteristics of the drying-induced strains in concrete. These studies illustrated that the DIC technique is promising for investigating the non-uniform deformations in cement-based materials.

In addition to the DIC technique, structure-based models also attracted much attention in studying the drying-induced non-uniform behaviour of cement-based materials. Grassl et al. [29], Idiart et al. [30], Maruyama et al. [21] and Havlásek et al. [31] used two-dimensional (2D) structure-based models to simulate drying-induced microcracks in concrete. Using a structure-based model, viz. the lattice fracture model, Schlangen et al. [32] obtained the non-uniform strains, stresses and cracks in concrete by considering the autogenous shrinkage of the cement paste. Further, Luković et al. [33] and Liu et al. [34,35] applied the lattice fracture modelling in predicting the drying-induced shrinkage and cracks of cement-based materials.

The external RH is an important parameter that influences the transport of moisture from concrete to environment [1]. Under different RH conditions, different drying-induced stresses form in concrete, leading to different levels of shrinkage and damage [36]. Hence, many studies focused on the effect of RH on the drying-induced shrinkage and damage in concrete. Bissonnette et al. [1], Baroghel-Bouny et al. [37] and Theiner et al. [38] investigated the influence of RH on the bulk drying shrinkage of concrete. Samouh et al. [36] evaluated the effect of RH on the cracking risk of concrete by using the ring test. However, very few studies quantified the effect of RH on the drying-induced damage in concrete by considering the non-uniform drying shrinkage behaviour in concrete.

The aim of this study was to quantify the effect of RH on the drying-induced damage in concrete in terms of the non-uniform drying shrinkage behaviour of concrete. First, the DIC technique was used to capture the displacements in concrete, which were applied to validate the lattice fracture model. Then, the validated lattice fracture model was used to obtain the patterns and areas of microcracks. A new damage index, which was calculated from the non-uniform strains determined using DIC, was proposed to evaluate the effect of RH on the drying-induced damage in concrete. The microcracks' patterns and areas obtained with the lattice fracture model were used to confirm the correlation between the new damage index and the dying-induced damage in concrete.

2. Experiments

2.1. Constituent materials and mix proportions of concrete

The component proportions, as listed in Table 1, were designed to produce C50 concrete (C50 represents the compressive strength of concrete can reach 50 MPa at 28 days since curing). The main raw materials were Type I 42.5 cement (also called ordinary Portland cement, and the compressive strength can reach 42.5 MPa at 28 days since curing), fine aggregates (fineness modulus = 2.8), coarse aggregates (5–10 mm and 16–20 mm) and water. The properties of the cement (e.g. chemical composition), fine aggregates (e.g. grading) and coarse aggregates (e.g. slit content) can be found in our previous work [16]. Mortar with the same water to cement ratio (W/C) as the concrete was also prepared (Table 1). The mortar's drying shrinkage was measured and used as input for the lattice fracture model. Mortar and concrete specimens with dimensions $100 \times 100 \times 100$ mm^3 were cast. Following the procedure in Bissonnette et al. [1], the specimens were demoulded after 1 day, and cured in a saturated calcium hydroxide solution at 23 °C for 28 days until testing.

2.2. DIC measurement

After curing in a saturated calcium hydroxide solution for 28 days, the mortar and concrete specimens were cut into 10-mm-thick slices by using a concrete cutting machine. The cutting speed was 200 r/min, and no significant cracks formed in the slices. The slices in the middle of specimens were used for the DIC measurement because the gravity might affect the spatial distribution of coarse aggregates on the top and bottom of concrete specimens. Then, stochastic speckle patterns were sprayed on the surface of the mortar and concrete slices, and the slices were placed in an isothermal chamber. The isothermal chamber's temperature was fixed at 20 °C and the RH was controlled at relatively high, medium, and low levels: 73%, 55% and 40%. At 0, 1, 3, 7, 11, 14, 28 and 60 days since drying (viz., 29, 30, 32, 36, 40, 43, 57, 89 days after casting), the mortar and concrete slices were removed from the isothermal chamber and observed using the DIC set-up (Fig. 1). Immediately after each observation, the slices were stored in the isothermal chamber again. In the DIC measurement, a serial of subsets was assigned on the surface of specimen. The displacement of each subset in the directions of the X axis (U) and Y axis (V) was determined by using mathematical correlation to analyse the digital images captured before and after the deformation. By differentiating U and V, the strains (ε_{xx}, ε_{yy} and ε_{xy}) of each subset in the X-Y plane were obtained ($\varepsilon_{xx} = \partial U/\partial x$, $\varepsilon_{yy} = \partial V/\partial y$ and $\varepsilon_{xy} = \partial U/\partial y + \partial V/\partial x$). Then, the maximum ($\varepsilon_{max}$) and minimum ($\varepsilon_{min}$) principal strains were calculated from these strains. The size of each subset was 0.05×0.05 mm^2 and the strain accuracy of the DIC set-up was 10 μm/m. More details of this DIC set-up and the concept of principal strains can be found in our previous study [16].

As schematically shown in Fig. 2, the bulk drying shrinkage of the specimen along X- and Y-axis was calculated by using Eqs. (1) and (2), respectively.

$$\varepsilon_{X,Bulk} = \frac{\sum(U_{Y1,i}/n_{Y1}) - \sum(U_{Y2,i}/n_{Y2})}{L} \tag{1}$$

Table 1
Mix proportions of mortar and concrete (kg/m^3).

Mix	Water	Type I 42.5 cement	Water to cement ratio	Fine aggregate	Coarse aggregate	
					5–10 mm	16–20 mm
Mortar	364	910	0.4	901	–	–
Concrete	222	554	0.4	541	433	649

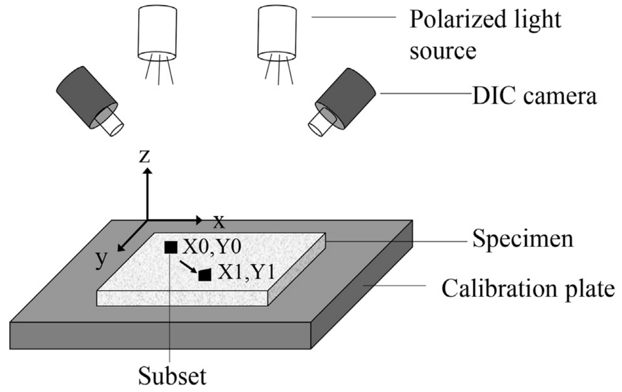

Fig. 1. Schematic diagram of the DIC set-up for determining the local deformations of specimen.

$$\varepsilon_{Y,Bulk} = \frac{\sum (V_{X1,i}/n_{X1}) - \sum (V_{X2,i}/n_{X2})}{L} \tag{2}$$

where $\varepsilon_{X,\ Bulk}$ and $\varepsilon_{Y,\ Bulk}$ are the bulk drying shrinkage of the specimen along the X- and Y-axis, respectively. n_{Y1} and n_{Y2}, n_{X1} and n_{X2} represent the number of the subsets on the edges along the Y- and X-axis, respectively. $U_{Y1,\ i}$ and $U_{Y2,\ i}$ represent the displacement of the subsets on the edges along the Y-axis. $V_{X1,\ i}$ and $V_{X2,\ i}$ represent the displacement of the nodes on the edges along the X-axis. L is the size of the specimen (100 mm).

The average bulk drying shrinkage of the specimen was calculated as:

$$\varepsilon_{Average,Bulk} = (\varepsilon_{X,Bulk} + \varepsilon_{Y,Bulk})/2 \tag{3}$$

2.3. Mechanical properties of the aggregate and mortar

The static elastic modulus and compressive strength of the coarse aggregates were determined using a nanoindenter. The loading and unloading were fixed at 3 mN/min, and the maximum load was 10 mN and held for 5 s. Based on the GB T50081–2002 standard [39], the static elastic modulus and compressive strength of the mortar specimen (100 × 100 × 100 mm^3) were determined after curing in a saturated calcium hydroxide solution for 28 days.

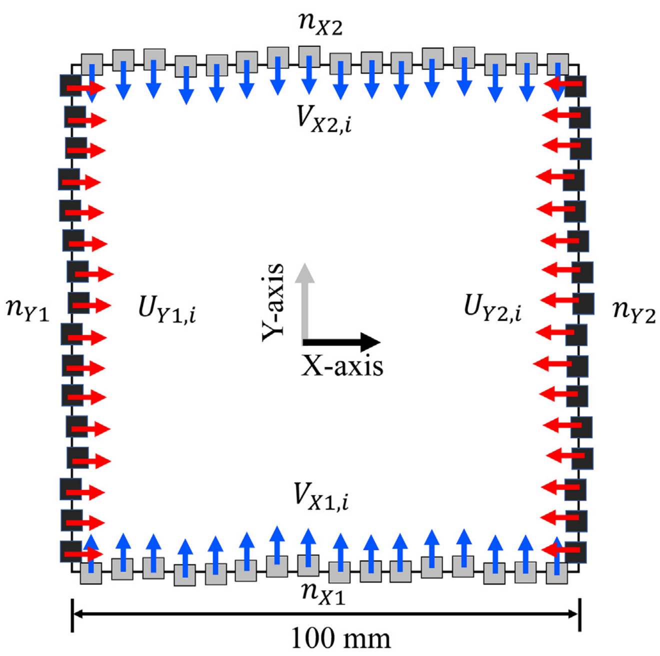

Fig. 2. Schematic diagram for calculating the bulk drying shrinkage of specimen.

3. Modelling approaches

A lattice fracture model called the generalized lattice analysis kernel (GLAK) was used to simulate the drying-induced deformations and microcracks in the concrete specimens. GLAK was developed by Delft University of Technology [40] and has been confirmed as a promising tool to predict the mechanical properties and fracture behaviour of cement-based materials [32–35,41,42]. In current study, the main inputs of GLAK were lattice mesh, imposing of drying-induced force, and boundary conditions. The main outputs of GLAK were non-uniform deformations and microcracks patterns.

3.1. Lattice mesh for GLAK

To compare the simulation results with the DIC observations, 2D lattice fracture modelling was used. At first, the digitalized 2D meso-structure of the concrete slice was obtained from the DIC photo (see Appendix A). Then, the lattice mesh for GLAK was obtained similar to the method of Luković, et al. [33] and Zhang et al. [41,42]. Mesh characteristics are important for lattice fracture model. The main mesh characteristics include the randomness, the shape, and the mechanical properties of mesh.

(1) Randomness

The digitized 2D meso-structure of the concrete slice was divided into square grids (250 × 250) of equal size (0.4 × 0.4 mm^2). Then, a sub-cell was assigned in the centre of each grid. A lattice node was randomly generated in each sub-cell, and designated as a coarse aggregate node or mortar node according to the main phase in the grid. The size ratio of sub-cells to grids can be used control the randomness of the mesh. In current study, this ratio was set as 0.5.

(2) Shape

Triangulation mesh is generally suitable for modelling the shrinkage of cement-based materials. In current study, the nodes were connected as lattice beam elements (the elements can resist axial and flexural loadings with six degrees of freedom) following the Delaunay triangulation algorithm. Depending on the type of connected nodes, these lattice beam elements were considered as coarse aggregate element, mortar element or interface element. The Delaunay triangulation lattice meshes constructed for various humidity levels are shown in Fig. 3. According to the data in Table 1 and [16], the volume fraction of coarse aggregates in the concrete was 0.4. The area fractions of the coarse aggregates in the lattice meshes shown in Fig. 3 were 0.40, 0.40, and 0.36 for 73%, 55%, and 40% RH, respectively. The area fraction of the coarse aggregates for 40% RH was not equal to 0.4 probably due to the variation of the coarse aggregates' spatial distribution in the concrete.

(3) Mechanical properties

Table 2 lists the mechanical properties of different element types, which were used as inputs for the lattice fracture model. The elastic modulus and compressive strength of the aggregate and mortar elements were obtained through the experiments as described in Section 2.3. Following Luković et al. [33] and Zhang et al. [42], the tensile strengths for the aggregate and mortar phases were set as 1/10 times the compressive strengths of the aggregate and mortar phases, respectively. In concrete, the interface between coarse aggregates and mortar phase generally shows smaller mechanical properties than the mortar phase due to the loose structure around the surface of coarse aggregates.

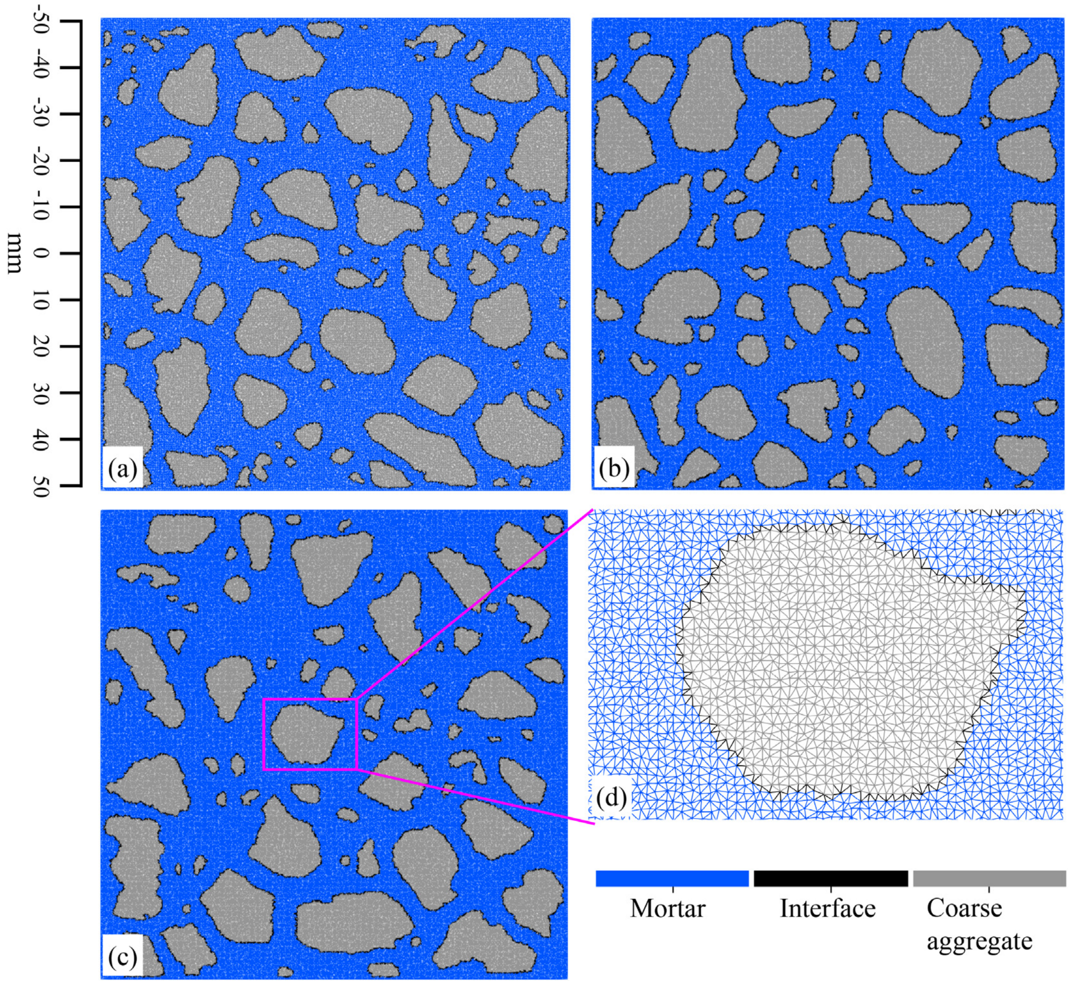

Fig. 3. Delaunay triangulation lattice meshes for 73% RH (a), 55% RH (b) and 40% RH (c): The area fractions of coarse aggregates are 0.40, 0.40, and 0.36 in (a), (b) and (c), respectively. (d) shows the zoom of an aggregate.

However, the mechanical properties of the interface are relatively difficult to be determined by experiments. In current study, the mechanical properties of the interface elements were empirically set according to the values reported in Luković et al. [33].

3.2. Local force imposed on lattice mesh

On a meso-scale, the local drying shrinkage of mortar phase exerts a local force to the concrete, which will cause the drying shrinkage of concrete. This local force (N_m) can be calculated from the drying shrinkage (ε_m) and elastic modulus (E_m) of the mortar phase according to Eq. (4) [33].

$$N_m = \varepsilon_m E_m A \tag{4}$$

where ε_m is the local drying shrinkage of the mortar phase in the concrete slice, E_m is the elastic modulus of the mortar phase. The elements were assumed to be circular, and the area of element's cross-section was defined as A. $\varepsilon_m E_m$ represents the local stress.

Table 2
Mechanical properties of lattice elements.

	Elastic modulus (GPa)	Compressive strength (MPa)	Calculated tensile strength (MPa)
Aggregate elements	80.0	90.0	9.0
Mortar elements	20.5	42.0	4.2
Interface elements	15.0	25.0	2.5

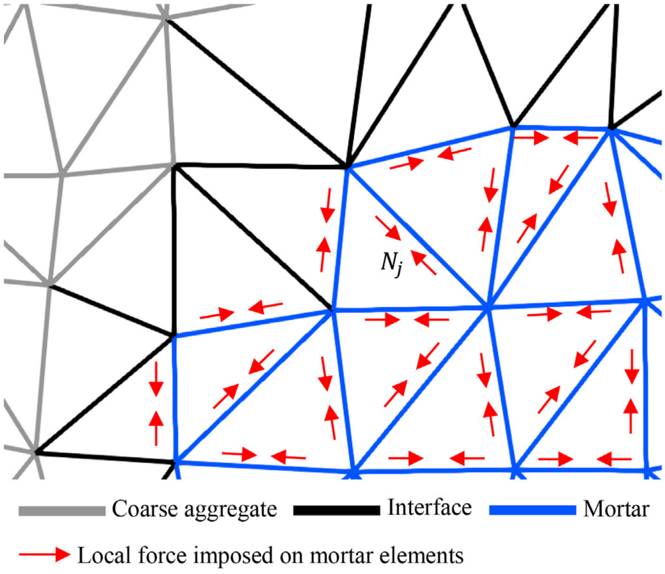

Fig. 4. Schematic diagram for imposing local force on mortar elements.

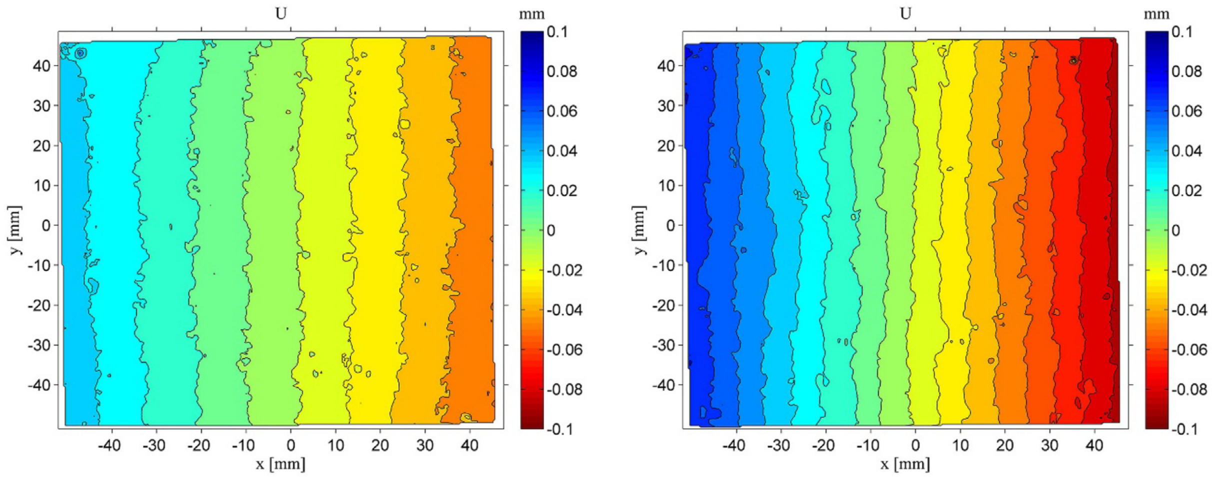

(a) 73% RH

(b) 55% RH

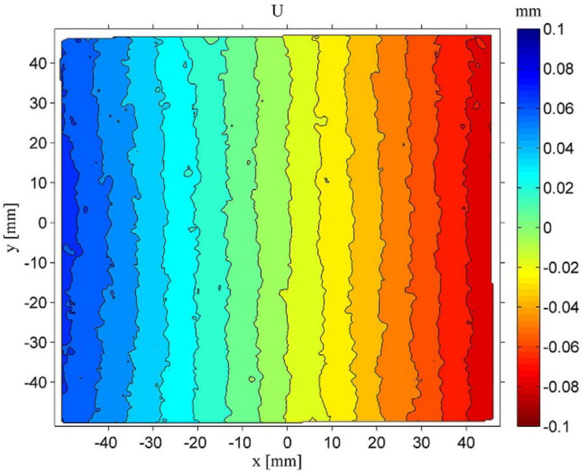

(c) 40% RH

Fig. 5. Measured displacement fields of mortar specimens along X-axis dried at 73%, 55% and 40% RH for 60 days.

For the mortar phase in the concrete slice, we assumed that the rate of moisture transport to the environment was close to that for the mortar slice under the same drying conditions. Hence, ε_m was considered as the total drying shrinkage of the mortar slice ($\varepsilon_{m,\ T}$), which was measured using the DIC technique.

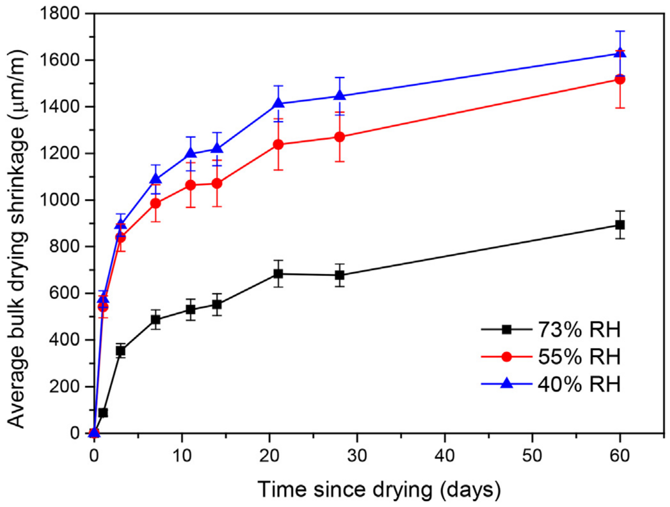

Fig. 6. Average bulk drying shrinkage of mortar specimens dried at 73%, 55% and 40% RH up to 60 days (obtained using DIC).

To simulate the drying-induced non-uniform behaviour of concrete on a meso-scale, the local force from the local drying shrinkage of mortar phase was imposed on the mortar elements using an iteration algorithm as follows: At step j, a force (N_j) was imposed on each mortar element (Fig. 4) causing the mortar elements to shrink. The shrinkage was restrained by other elements in the system, which resulted in tensile stresses in some elements of the lattice mesh. Then, the ratio ($\sigma_{t,\ element}/f_{t,\ element}$) of the formed tensile stress

Table 3
Local stress and force imposed on the mortar elements for the lattice fracture model.

Days	Imposed shrinkage stress (MPa, $\varepsilon_m E_m$)			Imposed shrinkage force (N, N_m)		
	73% RH	55% RH	40% RH	73% RH	55% RH	40% RH
1	1.79	11.11	11.78	0.24	1.47	1.55
3	7.27	17.20	18.30	0.96	2.27	2.42
7	9.99	20.22	22.31	1.32	2.67	2.94
11	10.86	21.81	24.55	1.43	2.88	3.24
14	11.31	21.97	24.97	1.49	2.90	3.30
21	14.02	25.37	28.96	1.85	3.35	3.82
28	13.88	26.05	29.62	1.83	3.44	3.91
60	18.32	31.11	33.37	2.42	4.11	4.40t

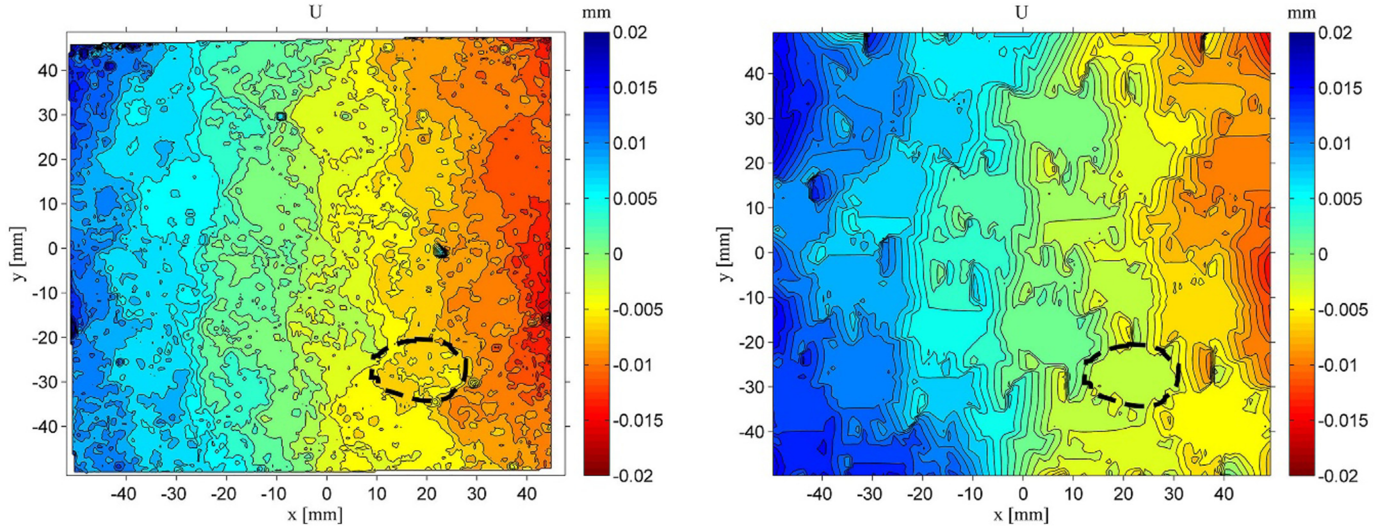

(a) 73% RH, DIC (b) 73% RH, lattice

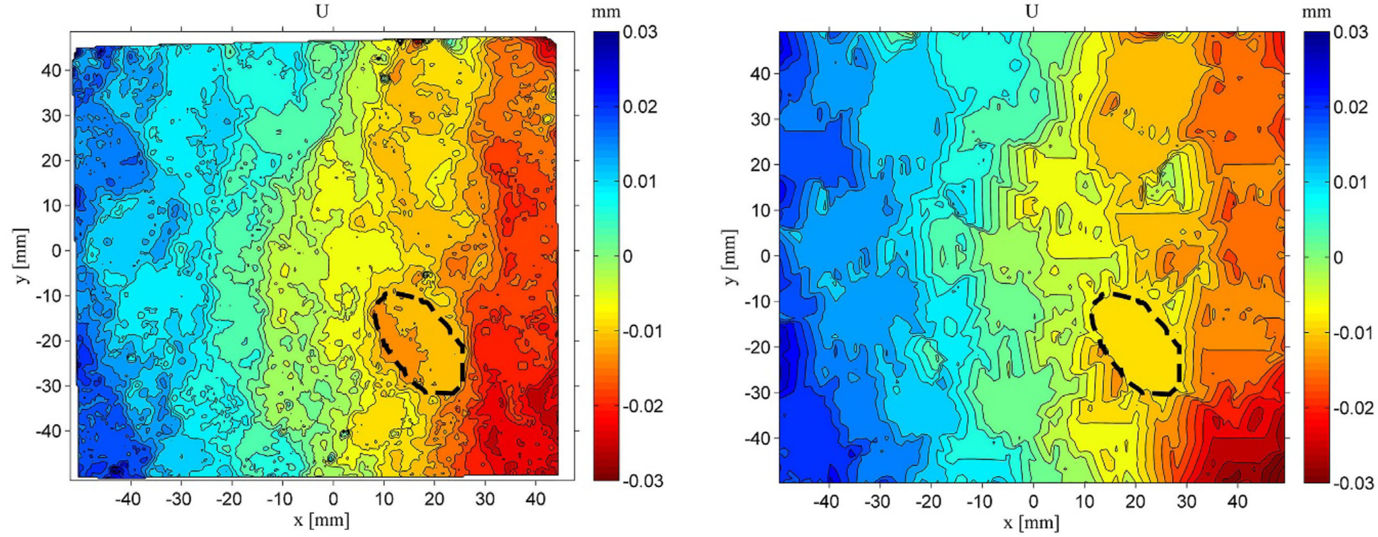

(c) 55% RH, DIC (d) 55% RH, lattice

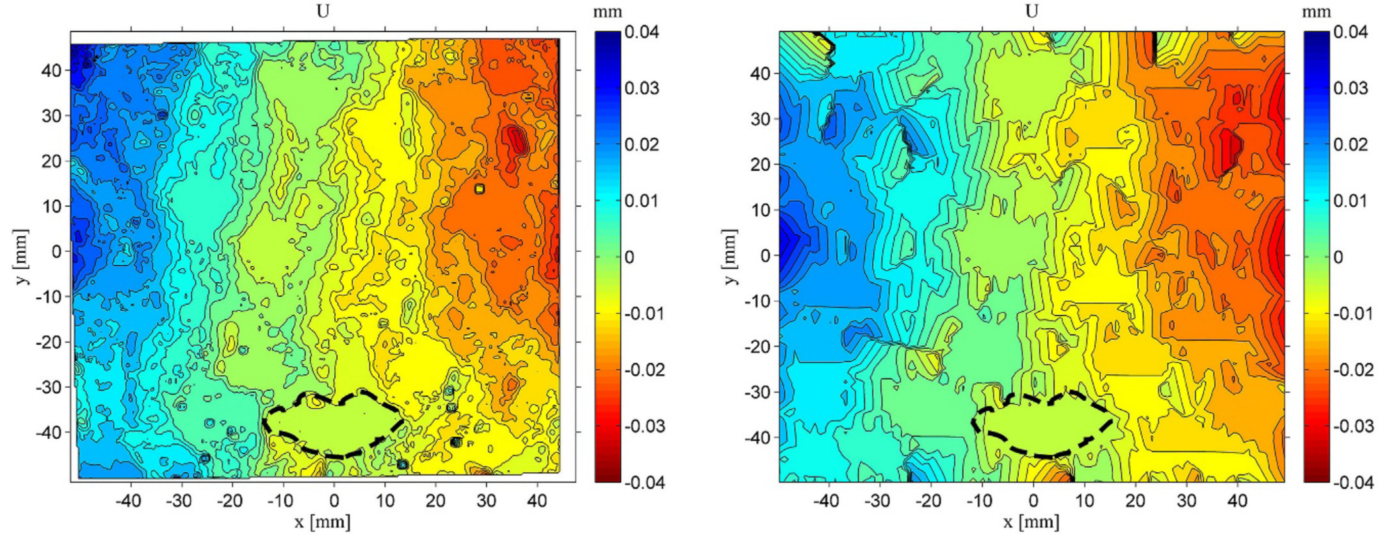

(e) 40% RH, DIC (f) 40% RH, lattice

Fig. 7. Displacement fields of concrete specimens along X-axis dried at 73%, 55% and 40% RH for 60 days: (a), (c) and (e) are from DIC; (b), (d) and (f) are from lattice fracture model.

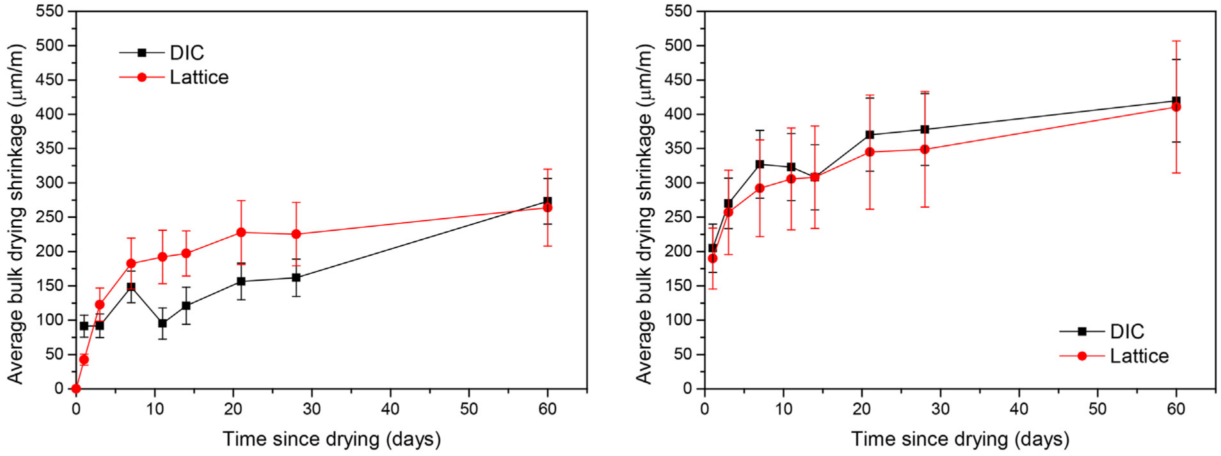

(a) 73% RH

(b) 55% RH

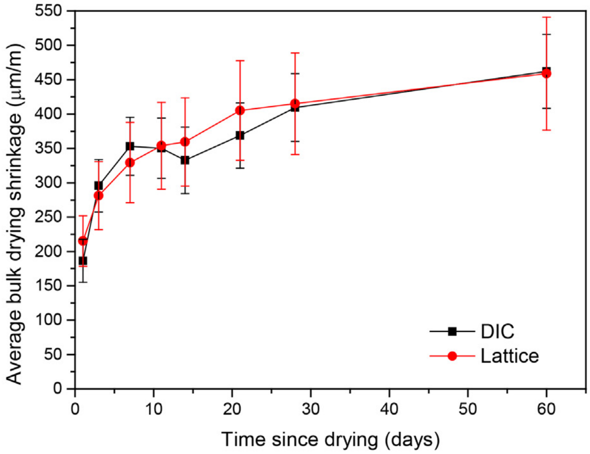

(c) 55% RH

Fig. 8. Average bulk drying shrinkage of concrete specimens dried at 73%, 55% and 40% RH for 60 days.

($\sigma_{t,\ element}$) in the element to the tensile strength ($f_{t,\ element}$) of the element was calculated. GLAK searched for the element with the largest value of $\sigma_{t,\ element}/f_{t,\ element}$, and N_j was increased until this element was broken. This iteration algorithm continued until N_j reached the local force N_m.

3.3. Boundary conditions

Four nodes in the centre of the lattice mesh were fixed. It was assumed that the coarse aggregate elements would not be broken.

3.4. Width and area of microcracks

In the lattice fracture modelling, a broken lattice element was defined as a microcrack. For a broken lattice element i, the width of the microcrack ($w_{i,\ j}$, μm) was calculated as the difference between the initial distance between the two nodes (l_i^0) and the distance between the two nodes at step j ($l_{i,\ j}{}'$). Notably, for a lattice element i broken at step j, the value of this microcrack's width was positive. However, if the distance between the two nodes became shorter at a further step k, the distance difference ($l_{i,\ j}{}' - l_i^0$) could become negative. However, the microcrack width is generally defined as positive in literature. To compare the microcrack width between this study and literature, $w_{i,\ j}$ was calculated as the absolute value of $l_{i,\ j}{}' - l_i^0$ (see Eq. (5)).

$$w_{i,j} = \left| l'_{i,j} - l_i^0 \right| \tag{5}$$

Using Eq. (6), the total area of the microcracks was calculated.

$$A_{Crack,j} = \frac{\sum_i (w_{i,j} \times l_c)}{A_{Concrete}} \times 10^3 \tag{6}$$

where $A_{Crack,\ j}$ is the total area of the microcracks per unit area of concrete (mm^2/m^2), l_c is the cross length of the lattice element (0.4 mm) and $A_{Concrete}$ is the total area of concrete (100 × 100 mm^2).

3.5. Influence of creep

Because cement-based materials generally exhibit viscoelastic characteristics, the drying-induced stress could cause the creep of cement-based materials [30,43]. This creep is called drying creep, and should be considered to predict the drying shrinkage of cement-based materials. As indicated by Bažant and Jirásek [44], the rate of nanoscale bond fractures in C-S-H gel will increase owing to the effect of drying-induced local stress, which is the main cause for the drying creep. In this study, the local force (N_m) imposed on the mortar elements was calculated from the total drying shrinkage of the mortar slice ($\varepsilon_{m,\ T}$), determined by using DIC. According to Grasley et al. [45], $\varepsilon_{m,\ T}$ equals to the

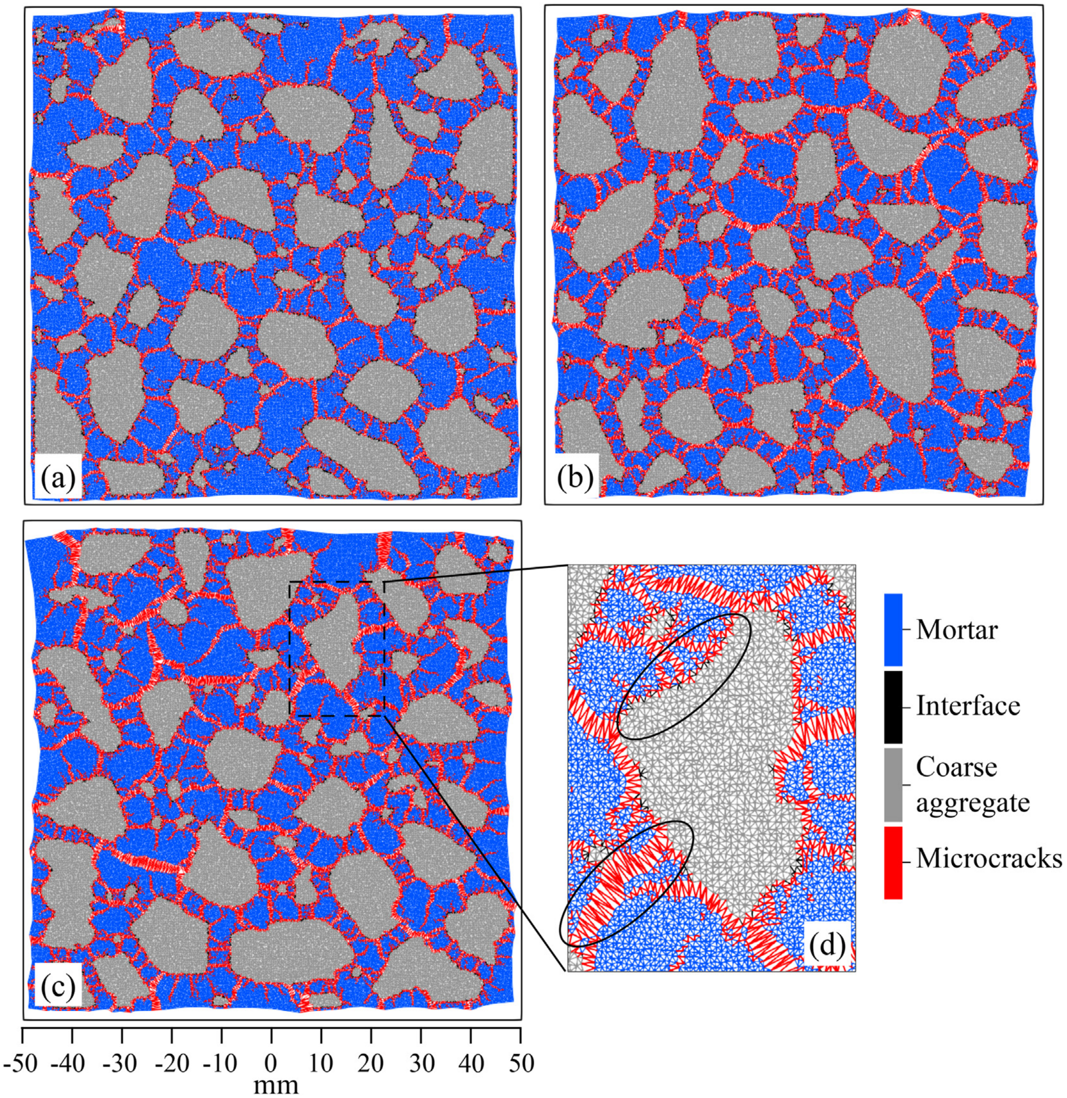

Fig. 9. Simulated drying-induced non-uniform deformations and micro-cracks of concrete specimens dried at 73% RH (a), 55% RH (b) and 40% RH (c and d); (d) shows the deformations magnified 100 times.

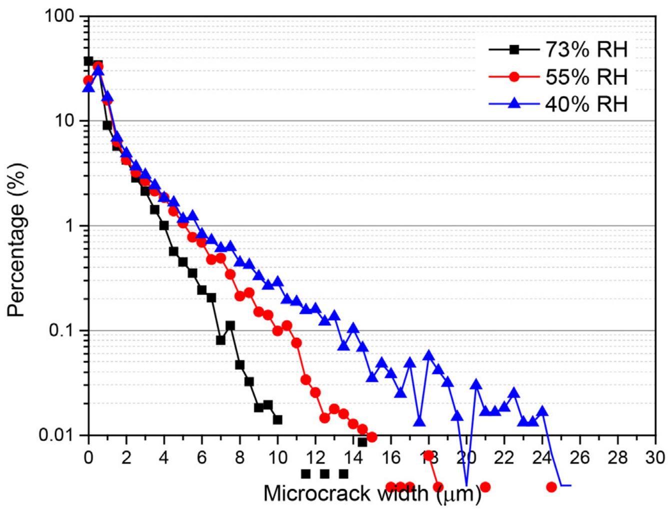

Fig. 10. Distributions of microcracks for concrete specimens dried at 73% RH, 55% RH and 40% RH for 60 days.

sum of true free shrinkage (ε_{sh}), drying creep (ε_{cr}) and remaining strain required for strain compatibility (ε_{el}). In other words, the influence of drying creep (ε_{cr}) on the non-uniform behaviour of concrete was considered by using $\varepsilon_{m,\,T}$ to calculate the local force (N_m) imposed on the mortar elements. However, due to the restraining effect of the coarse aggregates, the distribution of the stresses in the concrete slice would be different from that in the mortar slice. This part of drying creep was not involved in current study, which should be considered in further work.

4. Results and discussion

4.1. Displacement fields of mortar specimens

Fig. 5 shows the displacement fields of the mortar slices dried for 60 days along the X-axis (measured using the DIC set-up). The data along the Y-axis is shown in Appendix B. The blue and red represent the displacements towards the positive and negative directions of the axis, respectively. Notably, the moisture gradient could cause the differential shrinkage in cement-based materials, which might result in microcracks [46]. However, because the current study concerns the surface microcracking of concrete, slice specimens were used to reduce

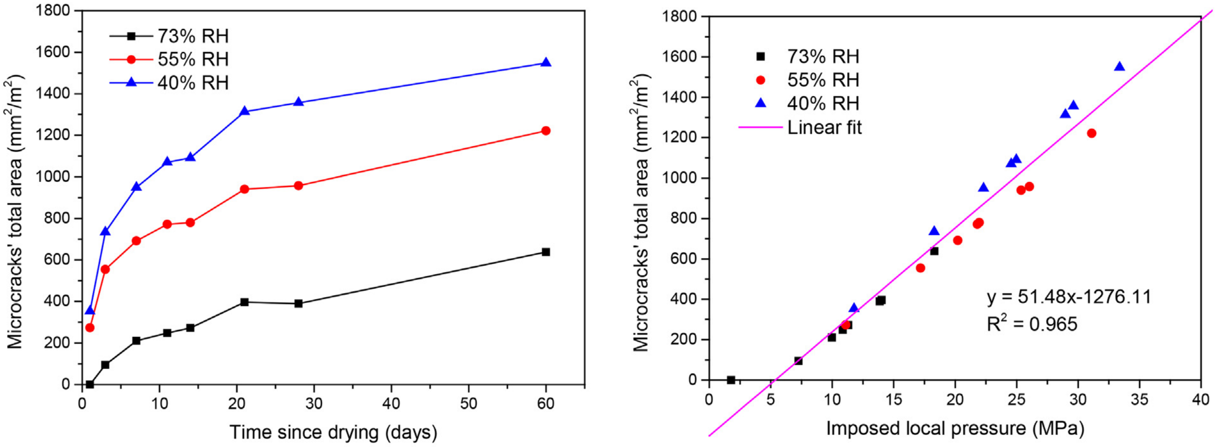

(a) (b)

Fig. 11. Total area of microcracks for concrete specimens dried at 73% RH, 55% RH and 40% RH up to 60 days: (a) Drying time versus microcracks' total area, (b) Imposed local pressure versus microcracks' total area.

the influence of moisture gradient on the drying shrinkage of specimens. As shown in Fig. 5a, b and c, the widths of colour strips are relatively uniform in each sub-figure, illustrating that the differential shrinkage along X-axis is not significant in the slice specimens. Similar observations can be found along Y-axis (see Appendix B).

Fig. 6 shows the average bulk drying shrinkage of the mortar specimens (obtained using the DIC). With decreasing the RH from 73% to 40%, the average bulk drying shrinkage of the mortar specimens (60 days since drying) increased from approximately 893 μm/m to 1627 μm/m, respectively.

Based on Eq. (4), the local force (N_m) imposed on the mortar lattice elements in the concrete specimens was calculated, wherein the parameters in Eq. (1): A (the area of elements' cross-section) and E_m (the elastic modulus of the mortar phase) were set as 0.132 mm^2 (this value was obtained by the calibration based on the elastic modulus of local phase and mesh) and 20.5 GPa, respectively. The results are presented in Table 3. With decreasing the RH from 73% to 40%, the total drying shrinkage of the mortar specimens decreased. Consequently, the local stress and force imposed on the mortar elements decreased.

4.2. Displacement fields of concrete specimens

Fig. 7a, c and d show the measured displacement fields of the concrete slices along the X-axis (the data along the Y-axis is shown in Appendix C). The displacement fields are notably non-uniform compared with Fig. 5. This is mainly caused by the restraining effect of coarse aggregates. In addition, some areas show similar displacement (e.g. the dashed areas in Fig. 7) because the coarse aggregates located in these areas. As shown in Fig. 7b, d and f, the simulated displacement fields are consistent with the DIC data.

Fig. 8 shows the average bulk drying shrinkage of the concrete specimens. As can be seen, both the data of DIC and lattice fracture modelling exhibit relatively large standard deviations (over 10% of the average bulk drying shrinkage of the concrete specimens). This is mainly because that the nodes on the edges of the concrete specimens deformed more heterogeneously than those on the edges of the mortar specimens. With ongoing drying and decreasing RH, the bulk drying shrinkage of the concrete specimens (determined with DIC) increased. To be more specific, for the concrete specimens dried at 73%, 55% and 40% RH from 1 day to 60 days since drying, the average bulk drying shrinkage of the concrete specimens increased from 91 μm/m to 273 μm/m, 206 μm/m to 406 μm/m, and 166 μm/m to 426 μm/m, respectively. The results of the lattice fracture modelling are consistent with the DIC data. With ongoing drying and decreasing RH, more moisture will be evaporated to external, which will increase the drying shrinkage of cement paste and mortar. On the scale of concrete, the bulk drying shrinkage of concrete will also increase.

4.3. Microcracks in concrete specimens

Fig. 9 shows the microcracks of the concrete specimens at 60 days since drying (simulated using the lattice fracture model), including a magnified view of simulated non-uniform deformations. With decreasing RH, the local force imposed on the mortar elements increased. Consequently, the deformations were larger and the microcracks became wider. Two types of microcracks can be identified in Fig. 9d: one is parallel to the aggregates and the other is normal to the aggregates. This is consistent with the experimental observations by Bisschop and van Mier [5,6], and Maruyama and Sasano [19].

The formation of these two types of microcracks depends on the distribution of stresses in the concrete. In the mortar phase around an aggregate, tangential tensile stresses will form owing to the shrinkage of the mortar phase. According to Goltermann [7,8], if the tangential tensile stresses exceed the tensile strength of the mortar, initial microcracks will form in the boundary phase. Then, the tangential tensile stresses will generate tensile microcracks perpendicular to the aggregate's surface. In addition, shear stress will develop in the interface and lead to shear microcracks parallel to the aggregate surface. Maruyama and Sasano [19] indicated that the shrinkage of the mortar phase between several aggregates will also result in the formation of microcracks parallel to the aggregate's surface.

The percentages of the microcracks with different widths are displayed in Fig. 10 (the microcrack-width interval is 0.5 μm, drying time is 60 days). The microcrack-width range are wider with decreasing RH, also because the lower RH is, the larger local force will be imposed on the mortar elements. For the concrete specimens dried at 73%, 55% and 40% RH, the microcrack-width ranges are 0–10.0 μm, 0–15.0 μm and 0–24.5, respectively. These ranges are consistent with those found in the literature. Wu et al. [47] quantified the drying-induced microcracks in concrete by using a fluorescent resin method and found that the concrete can reach equilibrium after drying at 21 °C and 55% RH for 10 months. The observed drying-induced microcracks were in the range of 1–60 μm, and 80% of the microcracks were smaller than 10 μm. Idiart et al. [30] determined the width of drying-induced microcracks in concrete using SEM, recording microcracks widths of 3–35 μm.

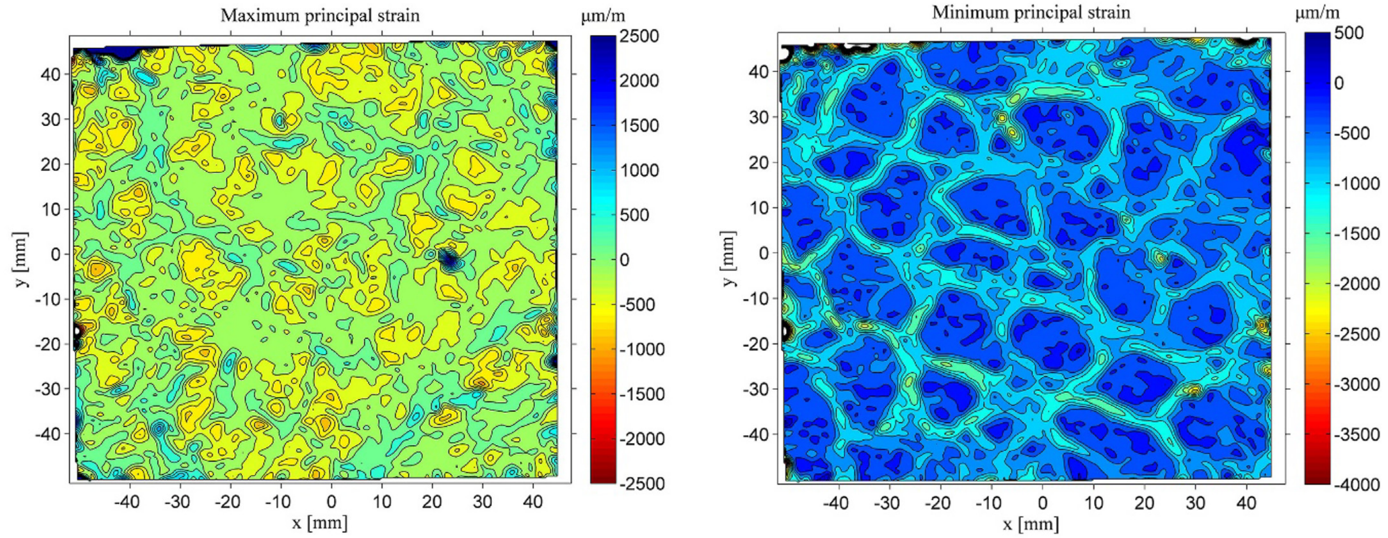

(a) 73% RH, ε_{max} (b) 73% RH, ε_{min}

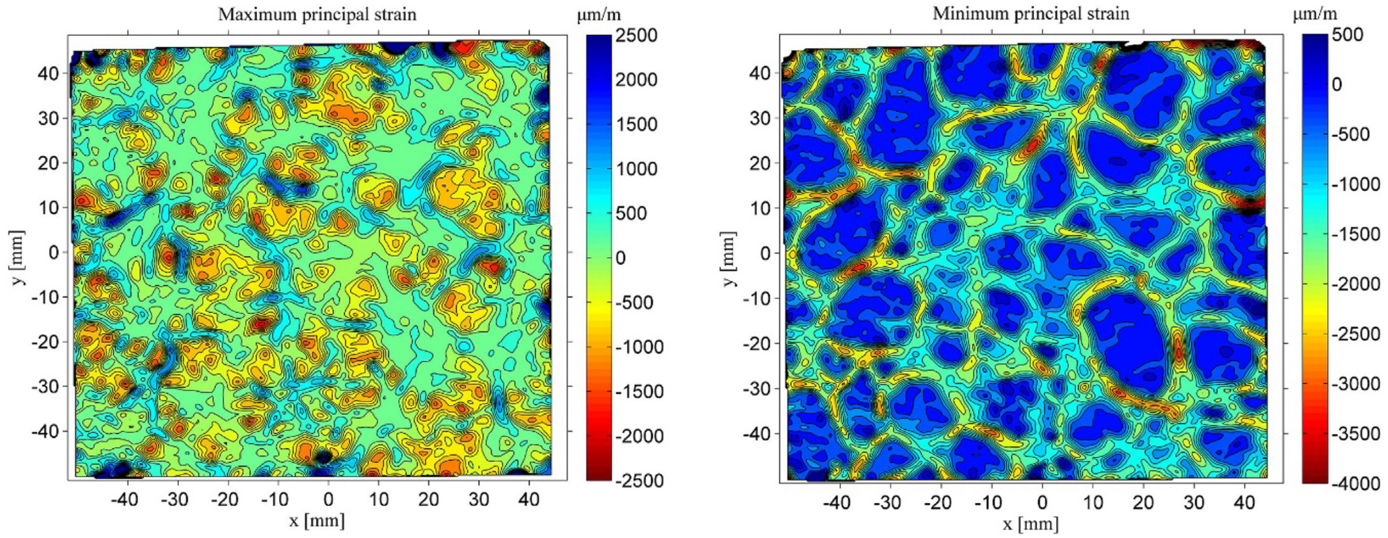

(c) 55% RH, ε_{max} (d) 55% RH, ε_{min}

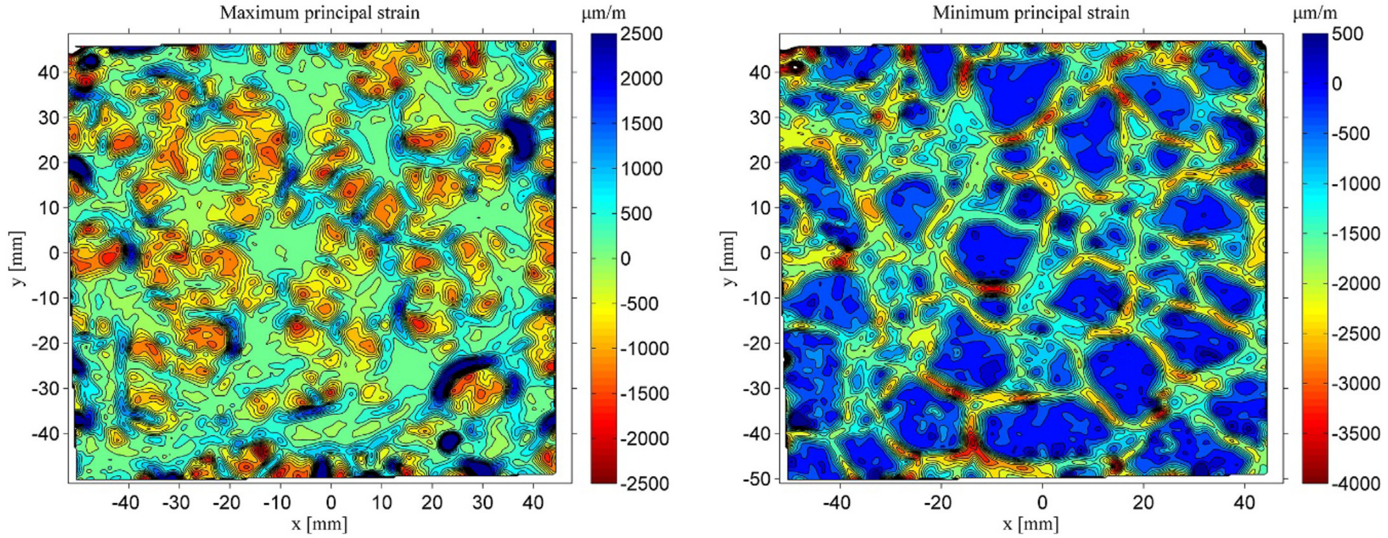

(e) 40% RH, ε_{max} (f) 40% RH, ε_{min}

Fig. 12. Principal strains of concrete specimens dried at 73% RH, 55% RH, and 40% RH for 60 days: (a), (c) and (e) are the maximum principal strains; (b), (d) and (f) are the minimum principal strains.

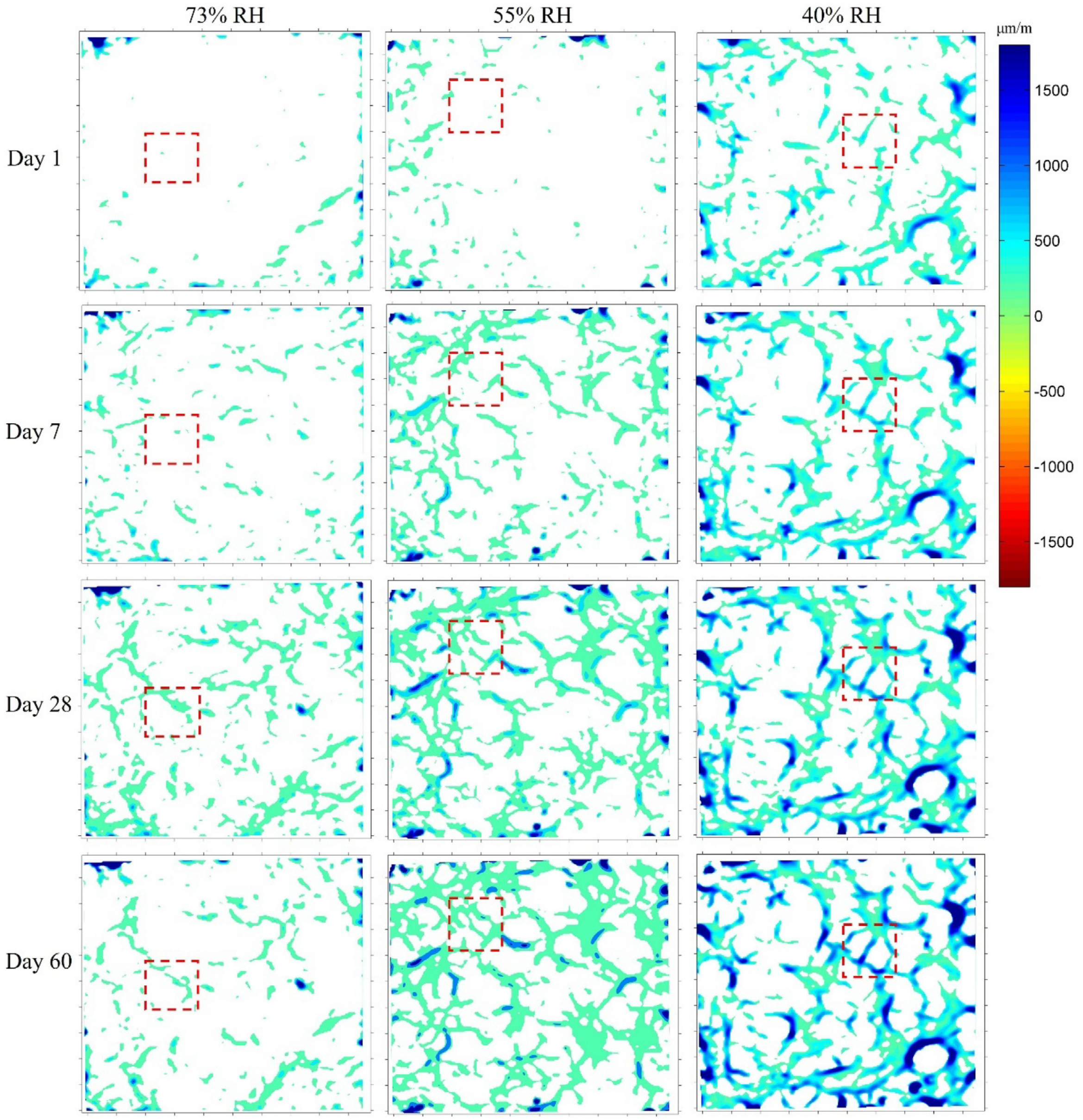

Fig. 13. Distribution of $\widetilde{\varepsilon} > K_0$ in the concrete specimens dried at 73% RH, 55% RH and 40% RH from day 1 to day 60.

The total area of microcracks was also calculated (Fig. 11). As exhibited in Fig. 11a, the RH significantly influence the microcracks' total area. It was also found that the microcracks' total area increased linearly as the local pressure imposed on the mortar elements increased (Fig. 11b). For example, with decreasing the RH from 73% to 40%, the local pressure imposed on the mortar elements increased from 18.32 MPa to 33.37 MPa, and the microcracks' total area increased from 637 mm^2/m^2 to 1548 mm^2/m^2.

4.4. Relationship between principal strains and microcracks

Fig. 12 shows the maximum (ε_{max}) and minimum (ε_{min}) principal strains of the concrete specimens obtained using the DIC. As shown in Fig. 12a, c and e, ε_{max} of the concrete specimens consist of tensile (positive value) and compressive (negative value) strains, while ε_{min} of the concrete specimens comprises mainly compressive strains (Fig. 12b, d and f). As will be discussed in the following paragraphs, the principal strains can be used to identify the drying-induced cracking patterns in concrete.

Mazars [48] described the damage of concrete structures. Owing to the importance of tensile strains in the damage of concrete, Mazars [48] introduced the concept of equivalent tensile strain ($\widetilde{\varepsilon}$) for evaluating the local intensity of tensile strains. $\widetilde{\varepsilon}$ was calculated from the positive part of ε_{max} and ε_{min} (Eq. (7)). It was suggested that if $\widetilde{\varepsilon}$ is larger than a certain tensile threshold, cracks will occur locally.

$$\widetilde{\varepsilon} = \sqrt{\langle \varepsilon_{max} \rangle_+^2 + \langle \varepsilon_{min} \rangle_+^2} \tag{7}$$

where $\widetilde{\varepsilon}$ is the equivalent strain and $\langle \varepsilon \rangle_+$ is the positive part operator for ε_{max} and ε_{min}.

Lagier et al. [17] captured the drying-induced strains of concrete using the DIC technique, and predicted the drying-induced cracking patterns based on the concept of equivalent strain, wherein the tensile threshold (K_0) was calculated from the tensile strength and elastic

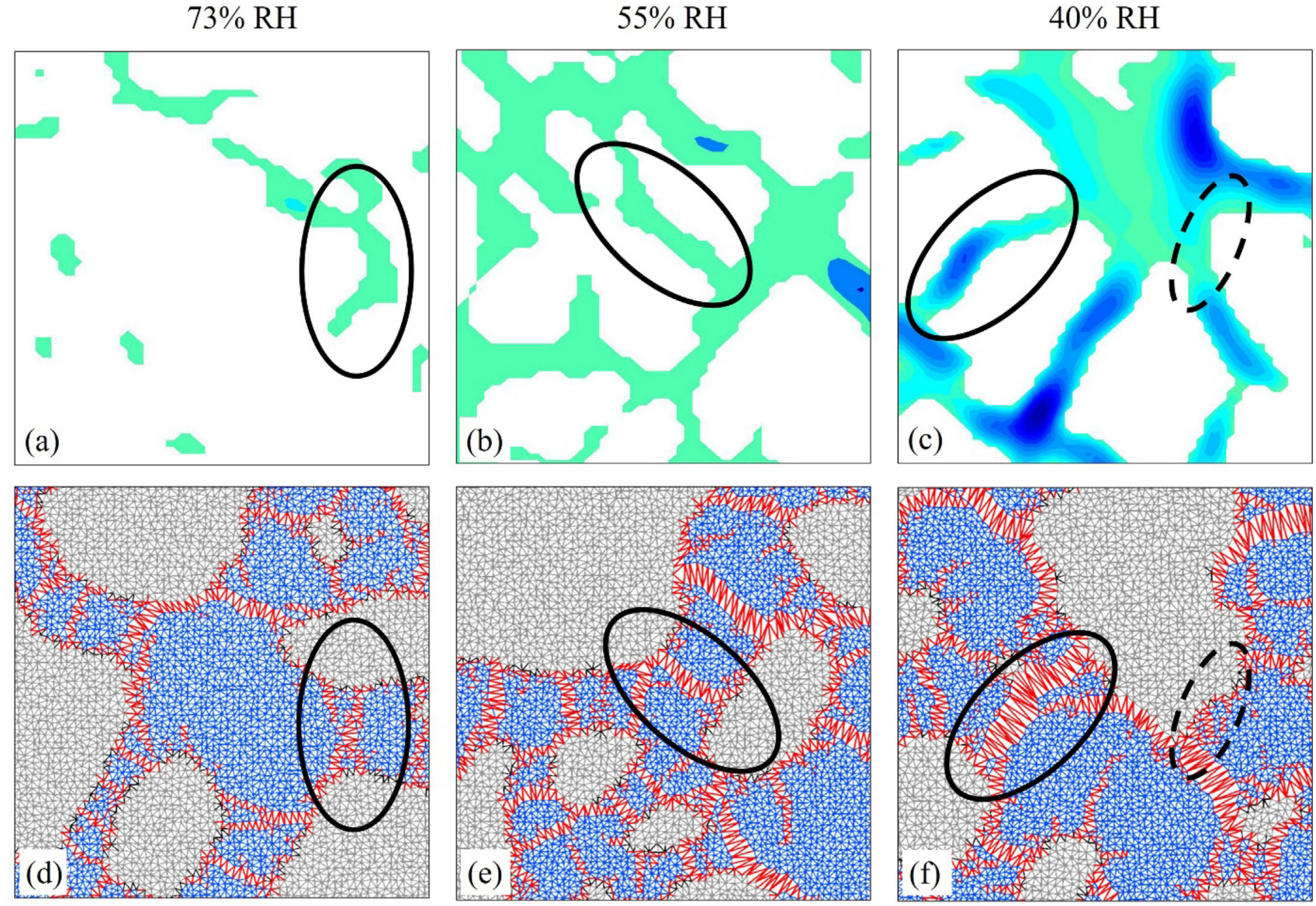

Fig. 14. Comparison between the distribution of $\widetilde{\varepsilon} > K_0$ and micro-cracks in the concrete specimens dried at 73% RH, 55% RH and 40% RH from 1 day to 60 days since drying; amplification is ×100.

modulus of the cement paste. The predicted cracking patterns were found to be consistent with the macro-observation. Similarly, Mauroux et al. [18] captured the drying-induced strains of coating mortars by using DIC. The concept of equivalent strain was also applied to predict the micro-cracking patterns in coating mortars. Most recently, Bertelsen et al. [28] used the DIC technique to monitor the plastic shrinkage behaviour of mortar specimens. Based on the concept of average strain, they evaluated the cracking patterns in mortar by considering the displacements and strains along the main axis.

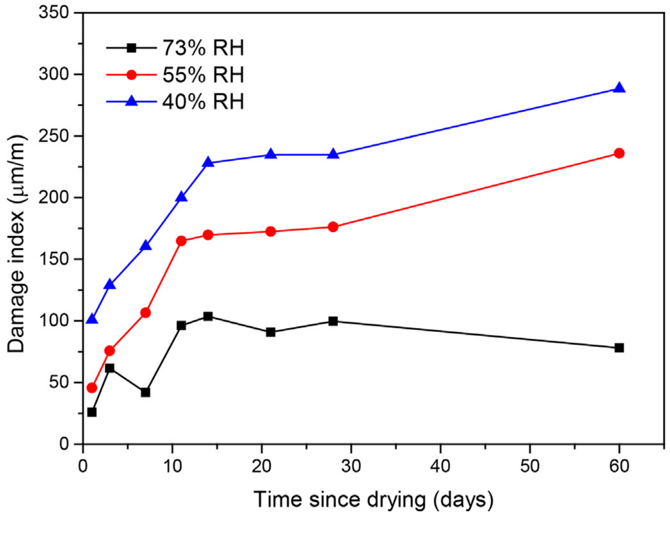

Fig. 15. Drying time versus damage index ($D_{\widetilde{\varepsilon}}$).

In present study, the concept of equivalent strain proposed by Mazars [48] was applied to assess the microcrack patterns from the DIC data as follows. First, Eq. (7) was used to calculate the $\widetilde{\varepsilon}$ of a subset. Following Lagier et al. [17], the tensile threshold (K_0) was calculated from the tensile strength ($f_{t,\,mortar}$) and elastic modulus (E_{mortar}) of mortar: $K_0 = f_{t,\,mortar}/E_{mortar}$=204 μm/m, based on the data listed in Table 2. Then, the distribution of $\widetilde{\varepsilon} > K_0$ in the concrete slices was plotted in Fig. 13. The area of $\widetilde{\varepsilon} > K_0$ increases not only with ongoing drying time from day 1 to day 60, but also with decreasing RH from 73% to 40%. Lagier et al. [17] and Mauroux et al. [18] considered the area of $\widetilde{\varepsilon} > K_0$ as the cracking indicator field. To directly compare the distributions of microcracks from the DIC data and the lattice modelling, we enlarged the local domains of the squares in Fig. 13. As shown in Fig. 14, some of the microcracks (obtained using the lattice fracture model) show good correlation with the distribution of $\widetilde{\varepsilon} > K_0$. Moreover, the two types of microcracks can also be identified in the distribution of $\widetilde{\varepsilon} > K_0$ (Fig. 14c and f). However, some of the simulated microcracks are not reflected in the distribution of $\widetilde{\varepsilon} > K_0$, probably due to the performance of the cameras used in the DIC set-up. Determined by the camera performance, the size of each subset was 0.05 × 0.05 mm^2 and the strain accuracy was 10 μm/m in current study. Hence, the strain fields corresponding to the very narrow microcracks may not be detected using this DIC set-up.

Maruyama and Sasano [19] proposed a damage index (D_ε) based on the positive part of the maximum principal strains (Eq. (8)). They showed that D_ε was related to the bulk drying shrinkage of concrete. However, because the threshold tensile strain was 0 μm/m in this damage index, D_ε overestimated the drying-induced damage.

$$D_\varepsilon = \frac{\sum_i \left(\varepsilon_{max,i} \cdot A_i | \varepsilon_{max,i} > 0\right)}{\sum_i A_i} \tag{8}$$

where A_i represents the area of subset i in the DIC measurement and $\varepsilon_{max,\,i}$ represents the maximum principal strain of the centre of subset i.

For a more accurate evaluation of the drying-induced damage in concrete, this study proposes a new damage index ($D_{\widetilde{\varepsilon}}$) that combines the concept of the equivalent strain of Mazars [48] and the damage index of Maruyama and Sasano [19]. $D_{\widetilde{\varepsilon}}$ can be expressed as:

$$D_{\widetilde{\varepsilon}} = \frac{\sum_i \left(\widetilde{\varepsilon}_i \cdot A_i | \widetilde{\varepsilon}_i > K_0\right)}{\sum_i A_i} \tag{9}$$

where $\widetilde{\varepsilon}_i$ represents the equivalent strain of subset i in the DIC measurement and K_0 represents the threshold strain, calculated from the tensile strength and elastic modulus of the mortar.

To determine the new damage index all the subsets with $\widetilde{\varepsilon} > K_0$ were considered (Eq. (9)). The $D_{\widetilde{\varepsilon}}$ calculated for the concrete specimens dried at 73% RH, 55% RH and 40% RH from 1 day to 60 days since drying are plotted in Fig. 15. As can be seen, the $D_{\widetilde{\varepsilon}}$ increases with decreasing RH. At 60 days since drying, the $D_{\widetilde{\varepsilon}}$ for 73% RH levelled off around 78 μm/m, while the $D_{\widetilde{\varepsilon}}$ for 55% RH and 40% RH increased to 235 μm/m and 288 μm/m, respectively, illustrating that the RH equal or lower than 55% might cause relatively high cracking risk to the concrete. This is mainly because the RH equal or lower than 55% result in relatively large drying shrinkage of mortar phase. This trend is consistent with that found in the literature. For example, Theiner et al. [38] reported that thin slices of concrete under 59% and 43% RH show significantly larger mass loss than those under 97%, 85% and 75% RH. Samouh et al. [36] determined the cracking time for concrete samples exposed to different RH levels by using the ring test, and reported that the 50% and 30% RH samples showed much shorter cracking time than the 70% RH one.

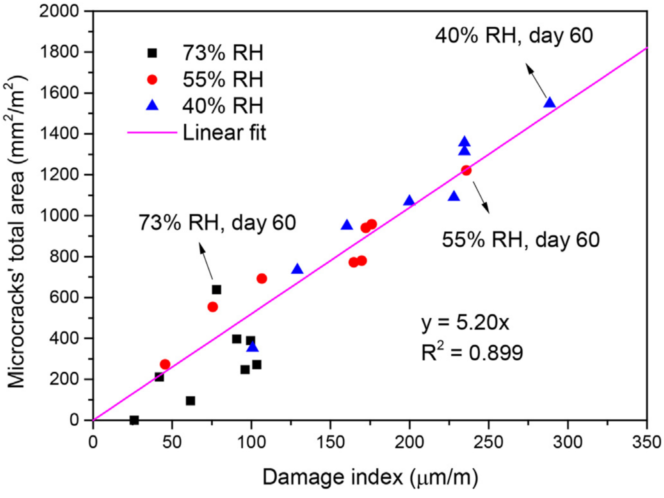

Fig. 16. Damage index ($D_{\widetilde{\varepsilon}}$) versus total area of microcracks.

To explore whether the $D_{\widetilde{\varepsilon}}$ (from the DIC) can directly reflect the dying-induced damage in concrete or not, the $D_{\widetilde{\varepsilon}}$ was plotted together with the total area of the simulated drying-induced microcracks in Fig. 16. As can be seen, the $D_{\widetilde{\varepsilon}}$ is proportional to the total area of the drying-induced microcracks, illustrating that the $D_{\widetilde{\varepsilon}}$ shows good correlation with the drying-induced damage of concrete. Based on this relationship, we can use the drying-induced deformations captured by the DIC technique to calculate the damage index, and quantify the drying-induced damage in the concrete.

As aforementioned, the strains induced by very narrow microcracks may not be detected owing to the resolution of the cameras used in the DIC set-up. As a result, the $D_{\widetilde{\varepsilon}}$ might be underestimated. In future work, the accuracy of the $D_{\widetilde{\varepsilon}}$ can be improved by improving the accuracy of the DIC cameras. In addition, the Mazars' definition of equivalent strain is suitable for applying the stress-related strains to identify the damage. However, the total strains determined using DIC probably comprises the stress-independent strains. These stress-independent strains might not be directly used to identify the damage based on the Mazars' definition of equivalent strain. How to consider these stress-independent strains in $D_{\widetilde{\varepsilon}}$ is another focus of further work.

5. Conclusions

The non-uniform shrinkage behaviour of concrete dried at 73 RH, 55% RH and 40% RH up to 60 days were systematically investigated by combining DIC and lattice modelling. The non-uniform deformations captured using DIC were used to validate the lattice fracture model. The influence of RH on the drying-induced damage was evaluated and quantified by combining the principal strains from DIC and the microcracks from the lattice fracture model. The following conclusions were drawn.

(1). For the concrete specimens dried at 73%, 55% and 40% RH from 1 day to 60 days since drying (30 days to 89 days since casting), the average bulk drying shrinkage obtained using the lattice fracture model increased from 42 μm/m to 263 μm/m, 190 μm/m to 410 μm/m, and 215 μm/m to 458 μm/m, respectively. These results are in good agreement with the DIC results (from 91 μm/m to 273 μm/m, 206 μm/m to 406 μm/m, and 166 μm/m to 426 μm/m for 73% RH, 55% RH and 40% RH, respectively).

(2). With decreasing the RH from 73% to 40%, the local pressure imposed on the mortar elements increased, which increased the simulated width of microcracks. The microcracks' total area increased linearly as the local pressure imposed on the mortar elements increased. At 60 days since drying (89 days since casting), the local pressure imposed on the mortar elements increased from 18.32 MPa to 33.37 MPa with decreasing the RH from 73% to 40%. Accordingly, the microcracks' maximum width and total area increased from 10 μm to 24.5 μm, and 637 mm^2/m^2 to 1548 mm^2/m^2, respectively.

(3). The distribution of the equivalent strain larger than the threshold tensile strength ($\widetilde{\varepsilon} > K_0$) showed good correlation with the simulated cracking patterns. A new damage index ($D_{\widetilde{\varepsilon}}$) was introduced by considering all the subsets with $\widetilde{\varepsilon} > K_0$. Under drying up to 60 days (89 days since casting), $D_{\widetilde{\varepsilon}}$ and the total area of the microcracks increased to 78 μm/m and 638 mm^2/m^2, 236 μm/m and 1222 mm^2/m^2, and 288 μm/m and 1548 mm^2/m^2 for 73%, 55% and 40% RH, respectively, illustrating that the RH equal or lower than 55% could result in a high cracking risk. Moreover, the $D_{\widetilde{\varepsilon}}$ was found to be proportional to the total area of the drying-induced microcracks. Based on this relationship, the drying-induced deformations captured using the DIC technique is attractive for the quantification of the drying-induced damage in concrete.

Data availability

The raw/processed data required to reproduce these findings cannot be shared at this time as the data also forms part of an ongoing study.

Declaration of Competing Interest

The authors declare that they have no known competing financial interests or personal relationships that could have appeared to influence the work reported in this paper.

Acknowledgements

This work was supported by the National Key Research and Development Program (2017YFB0310001-02), the National Natural Science Foundation of China (Grant No. 51672084, 51772103 and 51872097), and the China Postdoctoral Science Foundation funded project (Grant No. 2019M650199).

Appendix A. Method for obtaining digitized 2D meso-structure of concrete slice

In our previous study [16] we found that the coarse aggregates can be distinguished from the mortar phase in the ε_{min} image determined by using the DIC. In current study, the digitized 2D meso-structure of concrete slices were obtained as follows: As shown in Fig. A.1, the colour of the coarse aggregates in the ε_{min} image was changed to black (RGB value: 0, 0, 0) and the colour of the mortar in the ε_{min} image was changed to white (RGB value: 255, 255, 255). The threshold value for changing the colour image to grey image is 0.5.

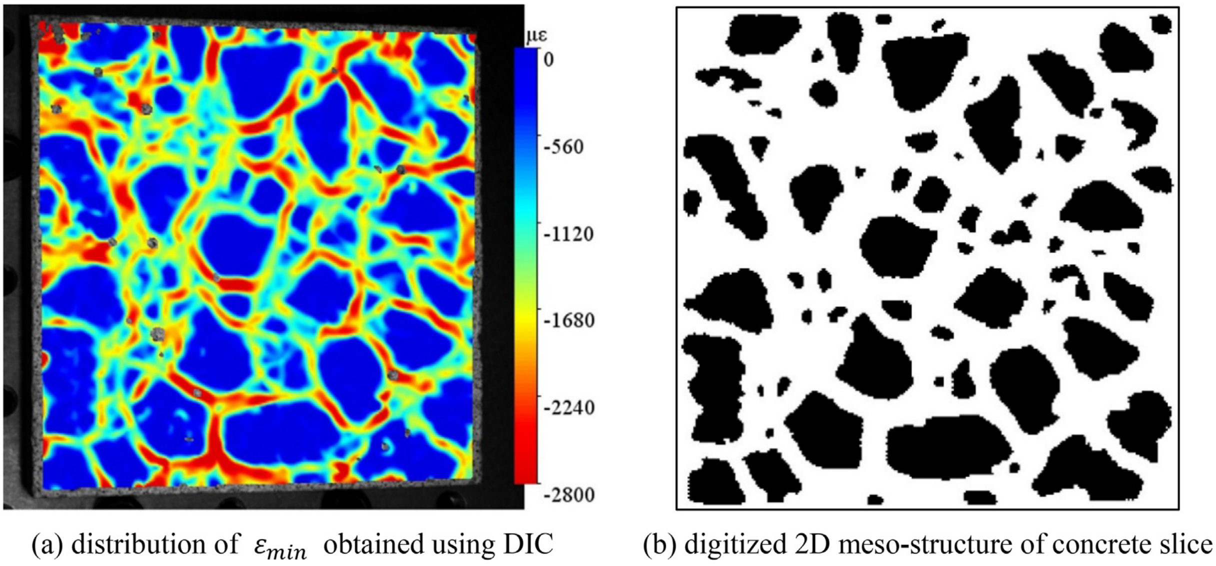

(a) distribution of ε_{min} obtained using DIC

(b) digitized 2D meso-structure of concrete slice

Fig. A.1. Digitized 2D meso-structure of concrete slice (100 × 100 mm^2) from ε_{min} measured with DIC.

Appendix B. Displacement fields of mortar specimens along Y-axis

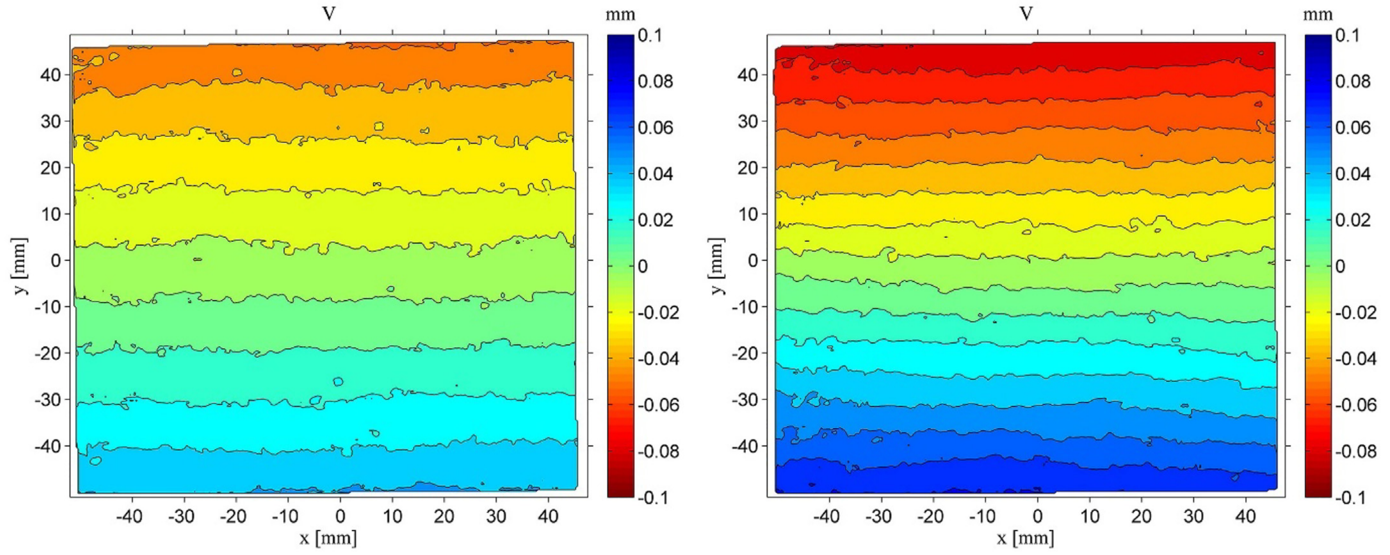

(a) 73% RH (b) 55% RH

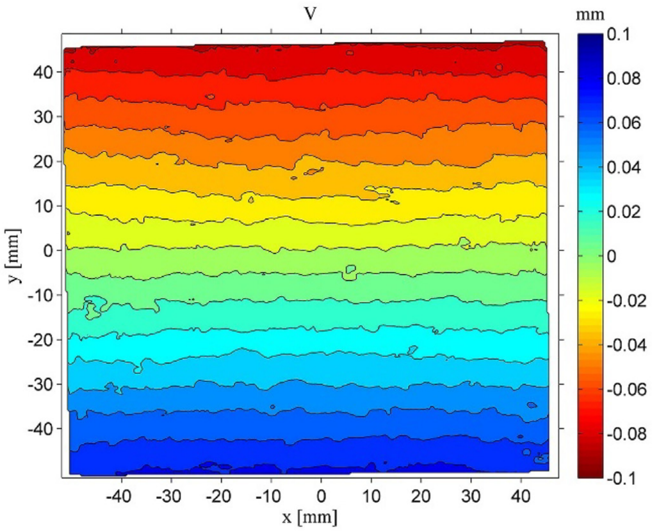

(c) 40% RH

Fig. B.1. Measured displacement fields of mortar specimens along Y-axis dried at 73% RH, 55% RH and 40% RH for 60 days since drying.

Appendix C. Displacement fields of concrete specimens along Y-axis

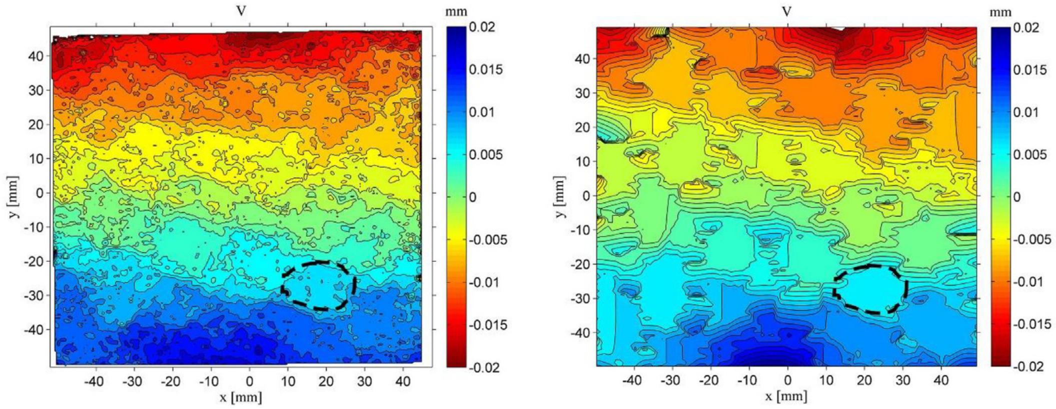

(a) 73% RH, DIC (b) 73% RH, lattice

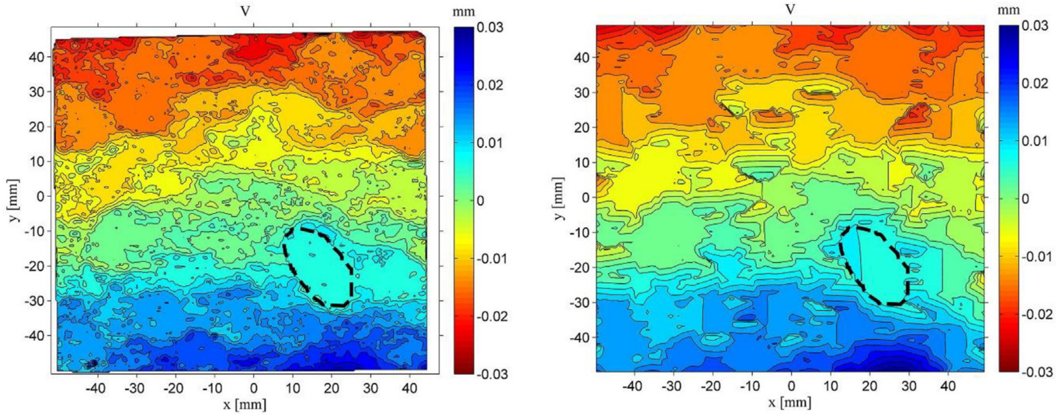

(c) 55% RH, DIC (d) 55% RH, lattice

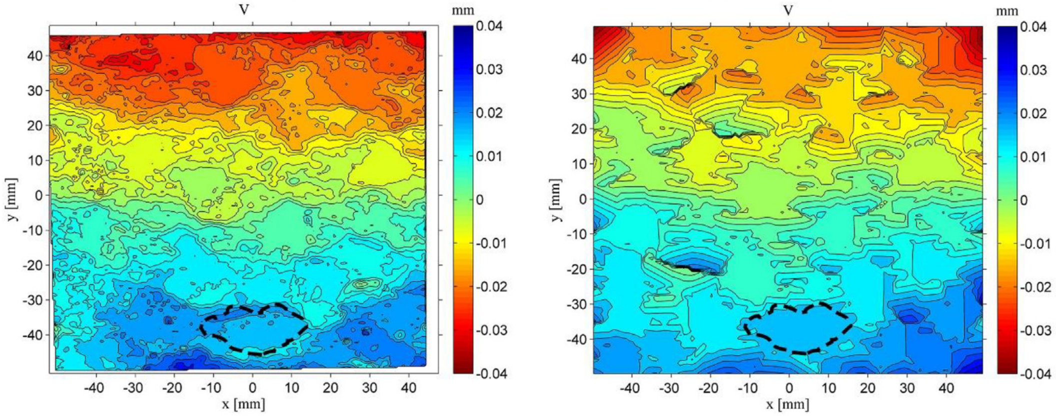

(e) 40% RH, DIC (f) 40% RH, lattice

Fig. C.1. Displacement fields of the concrete specimens along Y-axis dried at 73%, 55% and 40% RH for 60 days since drying: (a), (c) and (e) are from DIC; (b), (d) and (f) are from lattice fracture model.

References

[1] B. Bissonnette, P. Pierre, M. Pigeon, Influence of key parameters on drying shrinkage of cementitious materials, Cem. Concr. Res. 29 (1999) 1655–1662.

[2] H.M. Jennings, Colloid model of C-S-H and implications to the problem of creep and shrinkage, Mater. Struct. 37 (2004) 59–70.

[3] W. Hansen, Drying shrinkage mechanisms in Portland cement paste, J. Am. Ceram. Soc. 70 (1987) 323–328.

[4] P. Lura, O.M. Jensen, K. van Breugel, Autogenous shrinkage in high-performance cement paste: an evaluation of basic mechanisms, Cem. Concr. Res. 33 (2003) 223–232.

[5] J. Bisschop, J.G.M. van Mier, Effect of aggregates on drying shrinkage microcracking in cement-based composites, Mater. Struct. 35 (2002) 453–461.

[6] J. Bisschop, J.G.M. van Mier, How to study drying shrinkage microcracking in cement-based materials using optical and scanning electron microscopy, Cem. Concr. Res. 32 (2002) 279–287.

[7] P. Goltermann, Mechanical predictions on concrete deterioration. Part 1: eigenstresses in concrete, ACI Mater. J. 91 (1994) 543–550.

[8] P. Goltermann, Mechanical predictions of concrete deterioration. Part 2: classification of crack patterns, ACI Mater. J. 92 (1995) 58–63.

[9] C.M. Neubauer, H.M. Jennings, The use of digital images to determine deformation throughout a microstructure part I deformation mapping technique, J. Mater. Sci. 35 (2000) 5741–5749.

[10] M.A. Sutton, W. Wolters, W. Peters, W. Ranson, S. McNeill, Determination of displacements using an improved digital correlation method, Image Vis. Comput. 1 (1983) 133–139.

[11] W.H. Peters, W.F. Ranson, Digital imaging techniques in experimental stress analysis, Opt. Eng. 21 (1982) 427–431.

[12] I. Yamaguchi, Speckle displacement and decorrelation in the diffraction and image fields for small object deformation, Opt. Acta 28 (1981) 1359–1376.

[13] W.H. Peters, W.F. Ranson, M.A. Sutton, T.C. Chu, J. Anderson, Application of digital correlation methods to rigid body mechanics, Opt. Eng. 22 (1983) 38–42.

[14] M.N. Helfrick, C. Niezrecki, P. Avitabile, T. Schmidt, 3D digital image correlation methods for full-field vibration measurement, Mech. Syst. Signal P. R. 25 (2011) 917–927.

[15] B. Pan, H.M. Xie, L. Yang, Z.Y. Wang, Accurate measurement of satellite antenna surface using 3D digital image correlation technique, Strain 45 (2009) 194–200.

[16] Y. Chen, J. Wei, H. Huang, W. Jin, Q. Yu, Application of 3D-DIC to characterize the effect of aggregate size and volume on non-uniform shrinkage strain distribution in concrete, Cem. Concr. Compos. 86 (2018) 178–189.

[17] F. Lagier, X. Jourdain, C.D. Sa, F. Benboudjema, J.B. Colliat, Numerical strategies for prediction of drying cracks in heterogeneous materials: comparison upon experimental results, Eng. Struct. 33 (2011) 920–931.

[18] T. Mauroux, F. Benboudjema, P. Turcry, A. Aït-Mokhtar, O. Deves, Study of cracking due to drying in coating mortars by digital image correlation, Cem. Concr. Res. 42 (2012) 1014–1023.

[19] I. Maruyama, H. Sasano, Strain and crack distribution in concrete during drying, Mater. Struct. 47 (2014) 517–532.

[20] I. Maruyama, A. Sugie, Numerical study on drying shrinkage of concrete affected by aggregate size, J. Adv. Concr. Technol. 12 (2014) 279–288.

[21] I. Maruyama, H. Sasano, M. Lin, Impact of aggregate properties on the development of shrinkage-induced cracking in concrete under restraint conditions, Cem. Concr. Res. 85 (2016) 82–101.

[22] J.M. Kanema, J. Eid, S. Taibi, Shrinkage of earth concrete amended with recycled aggregates and superplasticizer: impact on mechanical properties and cracks, Mater. Des. 109 (2016) 378–389.

[23] Y. Zhao, L. Wang, Z. Lei, X. Han, Y. Xing, Experimental study on dynamic mechanical properties of the basalt fiber reinforced concrete after the freeze-thaw based on the digital image correlation method, Constr. Build. Mater. 147 (2017) 194–202.

[24] P. Zhao, A.M. Zsaki, M.R. Nokken, Using digital image correlation to evaluate plastic shrinkage cracking in cement-based materials, Constr. Build. Mater. 182 (2018) 108–117.

[25] A. Teramoto, M. Watanabe, R. Murakami, T. Ohkubo, Visualization of internal crack growth due to alkali–silica reaction using digital image correlation, Constr. Build. Mater. 190 (2018) 851–860.

[26] E.D. Dzaye, E. Tsangouri, K. Spiessens, G.D. Schutter, D.G. Aggelis, Digital image correlation (DIC) on fresh cement mortar to quantify settlement and shrinkage, Arch. Civ. Mech. Eng. 19 (2019) 205–214.

[27] Z. Huang, Y. Tu, S. Meng, C. Sabau, C. Popescu, G. Sas, Experimental study on shear deformation of reinforced concrete beams using digital image correlation, Eng. Struct. 181 (2019) 670–698.

[28] I.M.G. Bertelsen, C. Kragh, G. Cardinaud, L.M. Ottosen, G. Fischer, Quantification of plastic shrinkage cracking in mortars using digital image correlation, Cem. Concr. Res. 123 (2019) 105761.

[29] P. Grassl, H.S. Wong, N.R. Buenfeld, Influence of aggregate size and volume fraction on shrinkage induced micro-cracking of concrete and mortar, Cem. Concr. Res. 40 (2010) 85–93.

[30] A. Idiart, J. Bisschop, A. Caballero, P. Lura, A numerical and experimental study of aggregate-induced shrinkage cracking in cementitious composites, Cem. Concr. Res. 42 (2012) 272–281.

[31] P. Havlásek, M. Jirásek, Multiscale modeling of drying shrinkage and creep of concrete, Cem. Concr. Res. 85 (2016) 55–74.

[32] E. Schlangen, E.A.B. Koenders, K. van Breugel, Influence of internal dilation on the fracture behaviour of multi-phase materials, Eng. Fract. Mech. 74 (2007) 18–33.

[33] M. Luković, B. Šavija, E. Schlangen, G. Ye, K. Van Breugel, A 3D lattice modelling study of drying shrinkage damage in concrete repair systems, Materials 9 (2016) 575.

[34] L. Liu, X. Wang, H. Chen, C. Wan, M. Zhang, Numerical modeling of drying shrinkage deformation of cement-based composites by coupling multiscale structure model with 3D lattice analyses, Comput. Struct. 178 (2017) 88–104.

[35] L. Liu, X. Wang, H. Chen, C. Wan, Microstructure-based modelling of drying shrinkage and microcracking of cement paste at high relative humidity, Constr. Build. Mater. 126 (2016) 410–425.

[36] H. Samouh, E. Rozière, A. Loukili, Experimental and numerical study of the relative humidity effect on drying shrinkage and cracking of self-consolidating concrete, Cem. Concr. Res. (2019) 519–529.

[37] V. Baroghel-Bouny, M. Mainguy, T. Lassabatere, O. Coussy, Characterization and identification of equilibrium and transfer moisture properties for ordinary and high-performance cementitious materials, Cem. Concr. Res. 29 (1999) 1225–1238.

[38] Y. Theiner, M. Drexel, M. Neuner, G. Hofstetter, Comprehensive study of concrete creep, shrinkage, and water content evolution under sealed and drying conditions, Strain 53 (2017), e12223, .

[39] GB T50081−-2002, Standard for Test Method of Mechanical Properties on Ordinary Concrete, China Academy of Building Research, China, 2002.

[40] Z. Qian, E. Schlangen, G. Ye, K. Van Breugel, Prediction of mechanical properties of cement paste at microscale, Mater. Constr. 60 (2010) 7–18.

[41] H. Zhang, B. Šavija, S.C. Figueiredo, E. Schlangen, Experimentally validated multiscale modelling scheme of deformation and fracture of cement paste, Cem. Concr. Res. 102 (2017) 175–186.

[42] H. Zhang, Y. Xu, Y. Gan, Z. Chang, E. Schlangen, B. Šavija, Combined experimental and numerical study of uniaxial compression failure of hardened cement paste at micrometre length scale, Cem. Concr. Res. 126 (2019) 105925.

[43] Z.C. Grasley, C.K. Leung, Desiccation shrinkage of cementitious materials as an aging, poroviscoelastic response, Cem. Concr. Res. 41 (2011) 77–89.

[44] Z.P. Bažant, M. Jirásek, Creep and Hygrothermal Effects in Concrete Structures, Springer, Dordrech, The Netherlands, 2018.

[45] Z.C. Grasley, D.A. Lange, M.D.D. Ambrosia, Internal relative humidity and drying stress gradients in concrete, Mater. Struct. 390 (2006) 901–909.

[46] H. Samouh, E. Rozière, A. Loukili, The differential drying shrinkage effect on the concrete surface damage: experimental and numerical study, Cem. Concr. Res. 102 (2017) 212–224.

[47] Z. Wu, H.S. Wong, N.R. Buenfeld, Influence of drying-induced microcracking and related size effects on mass transport properties of concrete, Cem. Concr. Res. 68 (2015) 35–48.

[48] J. Mazars, A description of micro- and macroscale damage of concrete structures, Eng. Fract. Mech. 25 (1986) 729–737.